Title

Pulsed selective excitation theory and design in multiphoton MRI.

Permalink

https://escholarship.org/uc/item/42b2v0q7

Authors

Han, Victor

Chi, Jianshu

Ipek, Tanya

et al.

Publication Date

2023-03-01

DOI

10.1016/j.jmr.2023.107376

Peer reviewed

Pulsed selective excitation theory and design in multiphoton MRI

Victor Han[a,*], **Jianshu Chi**[a], **Tanya Deniz Ipek**[a], **Jingjia Chen**[a], **Chunlei Liu**[a,b]

[a]Department of Electrical Engineering and Computer Sciences, University of California, Berkeley, CA, USA

[b]Helen Wills Neuroscience Institute, University of California, Berkeley, CA, USA

Abstract

Excitation in MRI is traditionally done at the Larmor frequency, where the energy of each radiofrequency photon corresponds to the energy difference between two spin states. However, if multiple radiofrequencies are employed, then multiphoton excitation can also occur when the sum or difference of multiple photon frequencies equals the Larmor frequency. Although multiphoton excitation has been known since the early days of NMR, it has been relatively unexplored in MRI. In this work, equations and principles for multiphoton selective RF pulse design in imaging are presented and experimentally demonstrated. In particular, the case where there are radiofrequency fields in both the traditional xy-direction and non-traditional z-direction is considered. To produce the z-direction radiofrequency field, an additional uniform coil was added to a clinical MRI scanner. Using this coil, two-photon slice-selective pulses were designed to be equivalent to traditional pulses, producing similar excitation, slice profiles, and in vivo images. Being the result of a combination of multiple radiofrequency fields instead of just one, two-photon pulses have more flexibility in how their parameters can be changed. Although individual multiphoton excitations are less efficient than their traditional counterparts, when the z-direction radiofrequency field is spatially non-uniform, multiple multiphoton resonances can be simultaneously used at different locations to produce simultaneous multislice excitation with the same pulse duration but less tissue heating than a naive implementation. In particular, non-uniform z-direction radiofrequency fields with negligible added tissue heating provided by oscillating the MRI scanner's gradient fields at kilohertz frequencies were used to excite multiple slices simultaneously with less high-frequency xy-direction radiofrequency power. For an example three-slice excitation, we achieve half the xy-direction radiofrequency power compared to the naïve approach of adding three single-slice pulses. For conventional or unconventional applications, multiphoton excitation may be of interest when designing new MRI systems.

---

*Corresponding author at: Department of Electrical Engineering and Computer Sciences, University of California, Berkeley, 468 Cory Hall, Seat #17, Berkeley, CA 94720, USA. vhan@berkeley.edu (V. Han).

Keywords

Multiphoton; Two-photon; Selective excitation; Multislice; Multiband; SAR

---

1. Introduction

NMR excitation can occur not only at the Larmor frequency, but also at subharmonics of the Larmor frequency, a phenomenon called multiphoton excitation [1–4]. Although subharmonic excitation at high B_0 fields is very inefficient, the efficiency can be greatly increased by using multiple frequencies to generate excitation instead of a single subharmonic. When multiple RF fields (B_1 fields) are applied at different frequencies, multiphoton excitation can occur when the sums or differences of integer multiples of these frequencies equal the Larmor frequency [5,6]. With a proper choice of the RF frequencies, multiphoton excitation becomes practical in high-field MRI where specific absorption rate (SAR) may be a concern. In particular, SAR-negligible RF in the kilohertz range along the z-axis ($B_{1;z}$) can be combined with traditional RF in the xy-plane ($B_{1;xy}$) with proper frequency offset to create multiphoton excitation. In our previous work [7], we demonstrated the practicality of multiphoton excitation on a 3T clinical MRI scanner using fast oscillating gradients as the source of a spatially varying z-RF field, and showed that unintuitively, despite the general lower efficiency of multiphoton excitation, there can be SAR advantages when exciting multiple slices simultaneously. Simultaneous multislice excitations are used for simultaneous multislice (SMS) techniques [8–10], especially in the case where separation between slices allows for parallel imaging in the slice direction with little to no loss in SNR. Despite the advantage of accelerated imaging with reduced SNR penalty, a major drawback of SMS techniques is the increased SAR from the simultaneous multislice excitation.

In this work, we build on our previous work [7], describing the general principles of multiphoton pulsed selective excitation, providing a formalized treatment with design examples and implementations on a 3T scanner. There are two separate directions that this paper pursues: multiphoton excitation via spatially homogeneous z-RF fields and multiphoton excitation via spatially inhomogeneous z-RF fields. Whereas we only used oscillating gradients as a source of inhomogeneous z-RF in a 3T scanner in our previous work, here we also make use of an additional homemade coil providing homogeneous RF in the z-direction. With the additional z-direction coil, we demonstrate pulse design principles and additional flexibility, where the same excitation can be accomplished in several different ways with the same pulse duration. We also show the practicality of two-photon excitation with this additional coil for an in vivo head with excitation frequencies of 25 kHz in the z-direction and the Larmor frequency minus 25 kHz in the xy-direction, showing in vivo images in a very unique parameter regime.

While two-photon excitation with a homogeneous z-direction coil is likely to be useful only for non-standard applications such as frequency-isolated simultaneous transmit and receive [2,11], the examples with a homogeneous coil in this paper serve as a simpler case on which to build further ideas. We show how the theory and concepts from the homogeneous coil

case extend to non-homogeneous z-direction coils, which may be more useful for effective B_1 shimming with multiphoton pulses and SAR-efficient pulses. In particular, we revisit reduced SAR multiphoton multislice pulses using oscillating gradients. In our previous work [7], we only described reduced SAR simultaneous multislice adiabatic pulses. While adiabatic pulses are useful for invariance to RF amplitude, they have higher SAR than their non-adiabatic counterparts. Here, by using some extra tricks, we show the design of reduced SAR non-adiabatic multislice pulses with oscillating gradients. As an example, we reduce the SAR of a three-slice excitation by one-half compared to the naïve approach of adding three single-slice pulses. Such a pulse may find more widespread application for SMS techniques [8–10], helping to alleviate the SAR issues of the technique.

Whether for applications with extra hardware or for reduced SAR multislice RF pulses without extra hardware, we hope that the theory and design examples presented here can help guide multiphoton RF pulse design.

2.   Theory

We treat the spatial and temporal dynamics of multiphoton excitation using the Bloch equations for the purpose of designing general excitation pulses with single or multiple RF coils. In the following derivations, we will make use of several terms which are defined in Table 1. Note that based on the geometrical representation of the Schrödinger equation, the Bloch equations of vector rotations are equivalent to the quantum mechanical description in an ideal spin ½ system or any other ideal quantum mechanical two-level system [12].

2.1.   Bloch equations for multiphoton excitation

The Bloch equations can be written as

$$
\begin{bmatrix} \dot{M}_x \\ \dot{M}_y \\ \dot{M}_z \end{bmatrix} = \gamma \begin{bmatrix} 0 & B_z(t) & -B_y(t) \\ -B_z(t) & 0 & B_x(t) \\ B_y(t) & -B_x(t) & 0 \end{bmatrix} \begin{bmatrix} M_x \\ M_y \\ M_z \end{bmatrix} + \begin{bmatrix} -\dfrac{M_x}{T_2} \\ -\dfrac{M_y}{T_2} \\ -\dfrac{M_z - M_0}{T_1} \end{bmatrix}
$$

(1)

Ignoring relaxation and denoting the transverse magnetization

$$
m_{xy} = M_x + i M_y,
$$

(2)

and the transverse magnetic field as

$$
B_{xy} = B_x + i B_y,
$$

(3)

taking the derivative of Eq. (2) and substituting terms from Eqs. (1)–(3), the differential equation for the transverse component of the magnetization can be rewritten as

$$\frac{dm_{xy}}{dt} = i\gamma(M_z B_{xy} - m_{xy} B_z)$$

(4)

For pulsed B fields over the time period from 0 to T, Eq. (4) with initial condition $m_{xy}(\mathbf{r}, t = 0)$ can be solved with integrating factors to be [13,14]

$$m_{xy}(\mathbf{r}, T) = i\gamma \int_0^T M_z(\mathbf{r}, t) B_{xy}(\mathbf{r}, t) e^{-i\gamma \int_t^T B_z(\mathbf{r}, \tau)d\tau} dt$$

(5)

Eq. (5) describes the transverse magnetization resulting from excitation. Note that for small flip angles, $M_z(\mathbf{r}, t) \approx M_0$ and can be taken out of the integral for simplicity. The spatial and temporal profiles of the B fields provide the flexibility to design RF pulses that can optimize the excitation profiles. For simplicity, we assume that the RF coils generate spatially uniform fields with the addition of a linear gradient field. In addition to the standard RF coil in the xy-plane providing $B_{1,xy}$ fields, we also assume a RF coil in the z-direction providing $B_{1,z}$ fields. For additional flexibility, we also assume that the RF coil in the z-direction can provide nearly constant uniform magnetic fields $B_{DC,z}$. With these fields, in the Larmor frequency rotating frame,

$$\mathbf{B}_z = \mathbf{B}_{1,z}(t)\cos(\omega_z t + \phi(t)) + \mathbf{B}_{DC,z}(t) + \mathbf{G}(t) \cdot \mathbf{r},$$

(6)

$$\mathbf{B}_x = \mathbf{B}_{1,xy}(t)\cos((\omega_{xy} - \omega_0)t + \theta(t)),$$

(7)

$$\mathbf{B}_y = -\mathbf{B}_{1,xy}(t)\sin((\omega_{xy} - \omega_0)t + \theta(t)),$$

(8)

$$\mathbf{B}_{xy} = \mathbf{B}_{1,xy}(t)e^{-i((\omega_{xy} - \omega_0)t + \theta(t))}.$$

(9)

Under these conditions, Eq. (5) becomes

$$m_{xy}(\mathbf{r}, T) = i\gamma \int_0^T M_z B_{1,xy}(t) e^{-i((\omega_{xy} - \omega_0)t + \theta(t))} e^{-i\gamma \int_t^T B_{1,z}(\tau)\cos(\omega_z \tau + \phi(\tau))d\tau}$$
$$e^{-i\gamma \int_t^T B_{DC,z}(\tau)d\tau} e^{-i\gamma \int_t^T \mathbf{G}(\tau) \cdot \mathbf{r}d\tau} dt.$$

Under the condition of multiphoton excitation, $\omega_{xy} - \omega_0 = n\omega_z$ [7], Eq. (10) can be rewritten as

$$m_{xy}(\mathbf{r}, T) = i\gamma \int_0^T M_z B_{1,xy}(t) e^{-i(n\omega_z t + \theta(t))} e^{-i\gamma \int_t^T B_{1,z}(\tau)\cos(\omega_z\tau + \phi(\tau))d\tau}$$
$$e^{-i\gamma \int_t^T B_{DC,z}(\tau)d\tau} e^{i\mathbf{k}(t) \cdot \mathbf{r}} dt,$$

(11)

where $-\gamma \int_t^T \mathbf{G}(\tau)d\tau = \mathbf{k}(t)$ as in excitation k-space [15]. Eq. (11) shows that the contribution of a spatially uniform B_z pulse $e^{-i\gamma \int_t^T B_{1,z}(\tau)\cos(\omega_z\tau + \phi(\tau))d\tau} e^{-i\gamma \int_t^T B_{DC,z}(\tau)d\tau}$ can be equivalent to a phase/frequency modulation of the B_{xy} pulse, represented by $\theta(t)$. However, if ω_z is relatively large, bandwidth constraints in the RF system may make phase modulation of the B_{xy} pulse less practical. Phase modulating the B_{xy} pulse to achieve excitation would also cause the B_{xy} pulse to have a frequency component at the Larmor frequency, as expected since it is still standard one-photon excitation, which is not the case in multiphoton excitation. While it is not standard terminology, for conciseness in this manuscript, we refer to standard MRI excitation with only RF in the xy-plane as one-photon excitation.

2.2. Multiphoton selective excitation designs

2.2.1. Constant-$B_{1,z}$ pulses—If $B_{1,z}$ and ϕ are time invariant, i.e. a hard pulse, and assuming that $\omega_z \neq 0$, the integral involving $B_{1,z}(t)$ in Eq. (11) can be evaluated analytically as follows,

$$m_{xy}(\mathbf{r}, T) = i\gamma \int_0^T M_z B_{1,xy}(t) e^{-i(n\omega_z t + \theta(t))} e^{-i\frac{\gamma B_{1,z}}{\omega_z}(\sin(\omega_z T + \phi) - \sin(\omega_z t + \phi))}$$
$$e^{-i\gamma B_{DC,z}(T - t)} e^{i\mathbf{k}(t) \cdot \mathbf{r}} dt$$

$$m_{xy}(\mathbf{r}, T) = i\gamma e^{-i\frac{\gamma B_{1,z}}{\omega_z}\sin(\omega_z T + \phi)} e^{-i\gamma B_{DC,z}T}$$
$$\times \int_0^T M_z B_{1,xy}(t) e^{-i(n\omega_z t + \theta(t))} e^{-i\frac{\gamma B_{1,z}}{\omega_z}\sin(\omega_z t + \phi)} e^{i\gamma B_{DC,z}t} e^{i\mathbf{k}(t) \cdot \mathbf{r}} dt.$$

(13)

Using the Jacobi-Anger expansion shown below, where $J_m(-)$ is the Bessel function of the first kind of order m,

$$e^{i\frac{B_{1,z}}{w_z}\sin(\omega_z t + \phi)} = \sum_{m=-\infty}^{\infty} J_m\left(\frac{\gamma B_{1,z}}{\omega_z}\right) e^{im(\omega_z t + \phi)},$$

(14)

Eq. (13) can be rewritten as

$$m_{xy}(\mathbf{r}, T) = i\gamma e^{-i\frac{\gamma B_{1,z}}{\omega_z}\sin(\omega_z T + \phi)}e^{-i\gamma B_{DC,z}T}\int_0^T M_z B_{1,xy}(t)e^{-i(n\omega_z t + \theta(t))}$$

$$\left(\sum_{m=-\infty}^{\infty}J_m\left(\frac{\gamma B_{1,z}}{\omega_z}\right)e^{im(\omega_z t + \phi)}\right)e^{i\gamma B_{DC,z}t}e^{i\mathbf{k}(t)\cdot\mathbf{r}}dt \,.$$

(15)

For a given n, i.e. n z-photon excitation, the integral in Eq. (15) is only significant for the term involving m=n in that the fast oscillating terms mostly average out. If we assume that the bandwidths of time-varying terms are small relative to ω_z, Eq. (15) can be simplified as

$$m_{xy}(\mathbf{r}, T) = i\gamma e^{-i\left(\frac{\gamma B_{1,z}}{\omega_z}\sin(\omega_z T + \phi) - n\phi\right)}e^{-i\gamma B_{DC,z}T}J_n\left(\frac{\gamma B_{1,z}}{\omega_z}\right)$$

$$\int_0^T M_z B_{1,xy}(t)e^{-i\theta(t)}e^{i\gamma B_{DC,z}t}e^{i\mathbf{k}(t)\cdot\mathbf{r}}dt \,.$$

(16)

Eq. (16) shows that, if B_z is a hard pulse, it only adds a constant phase shift and amplitude scaling to the excitation. The slice profile and selection are determined entirely by B_{xy}. Like in the one-photon case, the slice location can be chosen by setting $\theta(t) = \Delta\omega t$, where $\Delta\omega$ is some frequency offset. While not commonly implemented in modern MRI but used historically, setting $B_{DC,z}$ to a non-zero value can also shift the slice.

Interestingly, in the multiphoton case, slice selection can also be achieved by shifting the frequency of B_z instead. Specifically, replacing ω_z with a new frequency of $\omega_z + \Delta\omega$ and assuming $B_{DC,z} = 0$, Eq. (10) becomes

$$m_{xy}(\mathbf{r}, T) = i\gamma\int_0^T M_z B_{1,xy}(t)e^{-i((\omega_{xy} - \omega_0)t + \theta(t))}e^{-i\gamma\int_t^T B_{1,z}(\tau)\cos((\omega_z + \Delta\omega)\tau + \phi)d\tau}$$

$$e^{-i\gamma\int_t^T \mathbf{G}(\tau)\cdot\mathbf{r}d\tau}dt$$

Then, following the same steps to Eq. (16) while keeping $\omega_{xy} - \omega_0 = n\omega_z$ so that the frequency of B_{xy} stays the same, we get

$$m_{xy}(\mathbf{r}, T) = i\gamma e^{-i\left(\frac{\gamma B_{1,z}}{\omega_z}\sin((\omega_z + \Delta\omega)T + \phi) - n\phi\right)}J_n\left(\frac{\gamma B_{1,z}}{\omega_z + \Delta\omega}\right)$$

$$\times\int_0^T M_z B_{1,xy}(t)e^{-i\theta(t)}e^{in\Delta\omega t}e^{i\mathbf{k}(t)\cdot\mathbf{r}}dt$$

(18)

The slice excitation location is determined by the frequency shift of $\Delta\omega$, the order of the multiphoton excitation, and the amplitude of the gradients. The effect is similar to choosing a different frequency for B_{xy} via $\theta(t)$.

We see that when we have access to a uniform B_z field, we are given three options for positioning a slice with multiphoton excitation: shifting the frequency of B_{xy}, adding a DC

B_z, or shifting the frequency of B_z. As a side note, since a DC or constant B_z field simply shifts the slice, the same should be true for a chemical shift.

2.2.2.   Shaped-B_z pulses—If $B_{1,z}(\tau)$ is slowly varying compared to $\cos(\omega_{1,z}\tau)$ and $\phi(\tau)$ is slowly varying compared to $\omega_{1,z}\tau$, then we can make some approximations that give us more design intuition than Eq. (11) in the general non-hard pulse case. We will make these assumptions more precise later. With the trigonometric identity

$$\cos(\omega_z\tau + \phi(\tau)) = \cos(\omega_z\tau)\cos(\phi(\tau))$$
$$-\sin(\omega_z\tau)\cos(\phi(\tau)),$$

(19)

we can rewrite Eq. (11) as

$$m_{xy}(\mathbf{r}, T) = i\gamma \int_0^T M_z B_{1,xy}(t)e^{-i(n\omega_z t + \theta(t))}$$
$$e^{-i\gamma \int_t^T B_{1,z}(\tau)(\cos(\omega_z\tau)\cos(\phi(\tau)) - \sin(\omega_z\tau)\sin(\phi(\tau)))d\tau}e^{-i\gamma \int_t^T B_{DC,z}(\tau)d\tau}e^{i\mathbf{k}(t) \cdot \mathbf{r}}dt,$$

(20)

Using integration by parts,

$$\int_t^T B_{1,z}(\tau)\cos(\omega_z\tau)\cos(\phi(\tau))d\tau$$
$$= \left[B_{1,z}(\tau)\cos(\phi(\tau))\frac{\sin(\omega_z\tau)}{\omega_z}\right]_t^T - \int_t^T \frac{\sin(\omega_z\tau)}{\omega_z}$$
$$\times \frac{d}{d\tau}[B_{1,z}(\tau)\cos(\phi(\tau))]d\tau$$

(21)

and

$$\int_t^T B_{1,z}(\tau)\sin(\omega_z\tau)\sin(\phi(\tau))d\tau$$
$$= \left[B_{1,z}(\tau)\sin(\phi(\tau))\frac{-\cos(\omega_z\tau)}{\omega_z}\right]_t^T - \int_t^T \frac{-\cos(\omega_z\tau)}{\omega_z}$$
$$\times \frac{d}{d\tau}[B_{1,z}(\tau)\sin(\phi(\tau))]d\tau$$

(22)

If the terms $\int_t^T \frac{\sin(\omega_z\tau)}{\omega_z}\frac{d}{d\tau}[B_{1,z}(\tau)\cos(\phi(\tau))]d\tau$ and $\int_t^T \frac{-\cos(\omega_z\tau)}{\omega_z}\frac{d}{d\tau}[B_{1,z}(\tau)\sin(\phi(\tau))]d\tau$ are negligible, then

$$\int_t^T B_{1,z}(\tau)(\cos(\omega_z\tau)\cos(\phi(\tau)) - \sin(\omega_z\tau)\sin(\phi(\tau)))d\tau$$

$$\approx \left[B_{1,z}(\tau)\cos(\phi(\tau))\frac{\sin(\omega_z\tau)}{\omega_z}\right]_t^T$$

$$-\left[B_{1,z}(\tau)\sin(\phi(\tau))\frac{-\cos(\omega_z\tau)}{\omega_z}\right]_t^T$$

$$= \frac{1}{\omega_z}(B_{1,z}(T)\sin(\omega_z T + \phi(T)) - B_{1,z}(t)\sin(\omega_z t + \phi(T)))$$

(23)

by the angle addition identity. Plugging this back in, Eq. (20) becomes

$$m_{xy}(\mathbf{r}, T) \approx i\gamma \int_0^T M_z B_{1,xy}(t$$

$$)e^{-i(n\omega_z t + \theta(t))}e^{-i\frac{\gamma}{\omega_z}(B_{1,z}(T)\sin(\omega_z T + \phi(T)) - B_{1,z}(t)\sin(\omega_z t + \phi(T)))}e^{xy} - i\gamma\int_t^T B_{DC,z}(\tau)d\tau e^{i\mathbf{k}(t)\cdot \mathbf{r}}_{dt}$$

(24)

Applying Eq. (14) like before,

$$m_{xy}(\mathbf{r}, T) \approx i\gamma \int_0^T M_z B_{1,xy}(t)e^{-i(n\omega_z t + \theta(t))}\left(\sum_{m=-\infty}^{\infty} J_m\left(\frac{\gamma B_{1,z}(t)}{\omega_t}\right)e^{im(\omega_z t + \phi(t))}\right)$$

$$e^{-i\frac{\gamma B_{1,z}(T)}{\omega_z}\sin(\omega_z T + \phi(T))}e^{-i\gamma\int_t^T B_{DC,z}(\tau)d\tau}e^{i\mathbf{k}(t)\cdot \mathbf{r}}_{dt}$$

(25)

This is just like Eq. (15), except that $J_m\left(\frac{\gamma B_{1,z}(t)}{\omega_z}\right)e^{im\phi(t)}$ and $B_{DC,z}(\tau)$ are also time-varying. If the bandwidth of $J_m\left(\frac{\gamma B_{1,z}(t)}{\omega_z}\right)e^{im\phi(t)}$ and the other time varying terms are small relative to $(m-n)\omega_z$, then like with Eq. (15), only the term with m=n contributes significantly to the integral. The fast oscillating off-resonant terms essentially average out in the integral, whereas the resonant term with m=n is much more important. This results in

$$m_{xy}(\mathbf{r}, T) \approx i\gamma \int_0^T M_z B_{1,xy}(t)e^{-i\theta(t)}J_n\left(\frac{\gamma B_{1,z}(t)}{\omega_t}\right)e^{-i\left(\frac{\gamma B_{1,z}(T)}{\omega_z}\sin(\omega_z T + \phi(T)) - n\phi(t)\right)}$$

$$e^{-i\gamma\int_t^T B_{DC,z}(\tau)d\tau}e^{i\mathbf{k}(t)\cdot \mathbf{r}}_{dt}$$

(26)

Eq. (26) shows that B_{xy} and B_z contribute to the excitation profile in a similar way with $B_{1,xy}(t)$ corresponding to $J_m\left(\frac{\gamma B_{1,z}(t)}{\omega_z}\right)$ and $e^{-i\theta(t)}$ corresponding to $e^{-i\left(\frac{\gamma B_{1,z}(T)}{\omega_z}\sin(\omega_z T + \phi(T)) - n\phi(t)\right)}e^{-i\gamma\int_t^T B_{DC,z}(\tau)d\tau}$, which represent amplitude and phase modulation respectively. So, amplitude and phase modulation can be done with B_{xy} or B_z independently, or with a combination of the two. Amplitude modulation via $B_{1,z}$ appears more complicated due to the Bessel function, but this is due to the asymmetry of the

setup. In the two-photon case where n, the number of z-photons involved, is one, J_1 is approximately linear for small values of $\frac{\gamma B_{1,z}(t)}{\omega_z}$. So, when our z-RF is like the standard xy-RF where the RF amplitude is very small compared to the frequency, the effective z-RF amplitude modulation is simply directly proportional to the actual amplitude modulation. However, for excitation efficiency, we often want to operate in the regime where $\gamma B_{1,z}(t)$ becomes comparable to ω_z and beyond. In this regime, J_1 takes the form of a dampened, aperiodic sine wave with a maximum value of about 0.58 at $\frac{\gamma B_{1,z}(t)}{\omega_z} = 1.84$. For higher order excitations with $n > 1$, for small values of $\frac{\gamma B_{1,z}(t)}{\omega_z}$ the Bessel functions are quadratic for $n = 2$, cubic for $n = 3$, etc. For larger values of $\frac{\gamma B_{1,z}(t)}{\omega_z}$, the higher order Bessel functions also become dampened, aperiodic sinusoids.

For phase modulation, the z-RF is very similar to the xy-RF, except that there is an extra constant term, and the phase modulation is multiplied by the number of z-photons involved, n. When $n = 1$ in the two-photon case, then z-RF phase modulation acts just like xy-RF phase modulation. When more z-photons are simultaneously involved, somewhat intuitively, they each contribute to the phase. When there is an additional coil producing z-direction magnetic fields, not only can the RF vary the phase, but the additional $B_{DC,z}$ term can also vary the phase.

2.2.3. Constant-$B_{1,xy}$ pulses—If B_{xy} is chosen as a hard pulse, Eq. (26) becomes

$$
m_{xy}(\mathbf{r}, T) \approx i\gamma B_{1,xy} e^{-i\theta} \int_0^T M_z J_n\left(\frac{\gamma B_{1,z}(t)}{\omega_z}\right)
$$
$$
e^{-i\left(\frac{\gamma B_{1,z}(T)}{\omega_z}\sin(\omega_z T + \phi(T)) - n\phi(t) + \gamma \int_t^T B_{DC,z}(t)d\tau\right)} e^{i\mathbf{k}(t)\cdot\mathbf{r}} dt
$$

$$(27)$$

We can observe correspondences between Eqs. (27) and (16). If B_{xy} is a hard pulse, it only adds a constant phase shift and amplitude scaling. The slice profile and selection are determined entirely by B_z. Slice position can still be changed with the same three options as described in Section 2.2.1.

2.3. Simultaneous multislice excitation

In conventional one-photon excitation, multiple slices can be excited simultaneously by modulating the B_{xy} field, e.g. by a trigonometric function. However, this approach increases the RF power and SAR deposition proportionally to the number of slices. With multiphoton excitation, we can shift the modulation to the B_z field. As the B_z field has orders of magnitude lower frequency, the resulting SAR increase is negligible. While a uniform B_z field or the corresponding frequency modulation of the B_{xy} field can distribute RF power to multiple frequencies, like the trigonometric modulation, neither have SAR benefits. Instead, a non-uniform B_z field can be used. In our previous work [7], we used fast oscillating gradients as a source of spatially linearly varying z-direction RF. With this approach, a single-frequency B_{xy} field produced by a transmit coil can excite multiple spatial locations

with different local Larmor frequencies using different multiphoton resonance conditions, thus reducing the need to increase transmit power. We previously used adiabatic pulses to compensate for the nonuniform excitation caused by spatially varying B_z field.

Here we analyze the design of non-adiabatic multiphoton multislice pulses more generally, but with ϕ as a constant for simplicity. Rewrite Eq. (6) as

$$B_z = (\mathbf{G}_{1,z}(t) \cdot \mathbf{r} + B_{1,z}(t))\cos(\omega_z t + \phi) + \mathbf{G}(t) \cdot \mathbf{r}$$

(28)

Now B_z consists of a uniform RF field as well as gradient fields, produced by the same physical coils, split between a slowly-varying component ($\mathbf{G}$) and an oscillating component with frequency of ω_z ($\mathbf{G}_{1,z}$). With Eq. (28), Eq. (10) becomes

$$m_{xy}(\mathbf{r}, T) = i\gamma \int_0^T M_z B_{1,xy}(t) e^{-i((\omega_{xy} - \omega_0)t + \theta(t))}$$
$$e^{-i\gamma \int_t^T (\mathbf{G}_{1,z}(\tau) \cdot \mathbf{r} + B_{1,z}(\tau))\cos(\omega_z \tau + \phi)d\tau} e^{i\mathbf{k}(t) \cdot \mathbf{r}}dt$$

(29)

If we design the RF pulses such that 1) $\omega_{xy} = \omega_0$, and 2) $\mathbf{G}_{1,z}(t) \cdot \mathbf{r} + B_{1,z}(t)$ varies much more slowly than $\cos(\omega_z t + \phi)$, then, by applying the Jacobi-Anger expansion as in previous sections, Eq. (29) becomes

$$m_{xy}(\mathbf{r}, T) \approx i\gamma \int_0^T M_z \sum_{m=-\infty}^{\infty} J_m\left(\frac{\gamma(\mathbf{G}_{1,z}(t) \cdot \mathbf{r} + B_{1,z}(t))}{\omega_z}\right)$$
$$B_{1,xy}(t) e^{im\omega_z t} e^{-1\left(\frac{\gamma(\mathbf{G}_{1,z}(T) \cdot \mathbf{r} + B_{1,z}(T))}{\omega_z}\sin(\omega_z T + \phi) - m\phi\right)} e^{-i\theta(t)} e^{i\mathbf{k}(t) \cdot \mathbf{r}}dt$$

(30)

Each discrete frequency ($m\omega_z$) permits the selective excitation of a slice. The amplitudes of these frequencies (J_m) are spatially dependent, which allows for reduced SAR, as described before, while the uniform W:\Production\20042\025055MC\0001\Graphics term allows for more flexibility to control the spatial dependence. Without the uniform term, only one-photon excitation could have a contribution at the isocenter because for r = 0 and $B_{1,z}(t) = 0$, we would have $\sum_{m=-\infty}^{\infty} J_m(0) B_{1,xy}(t) e^{im\omega_z t} e^{im\phi} = J_0(0) B_{1,xy}(t)$ as Bessel functions are zero at zero except for the 0th order. If a uniform $B_{1,z}$ field is not available, $\theta(t)$ can be utilized instead to perform the same function, as shown in Section 2.1. Without any compensation, the various J_m terms are likely not equal, thus producing slices with unequal flip angles. An example method of equalizing the flip angles is given for example parameters in Section 3.6.

3. Methods

3.1. Overview of pulse design and simulation

To demonstrate the principles described in the theory, we simulated and implemented five sets of related pulses, each set demonstrating a different principle. The first three sets utilized a uniform B_z field provided by an additional coil, while the last two sets demonstrated multislice excitation with oscillating gradients and no additional hardware. Simulations based on Eq. (1) were written in Python and the code is available at https://github.com/LiuCLab/multiphoton-selective-excitation. To generate each pulse in the first three sets, the following procedure was followed.

1. Generate a prototype pulse together with gradients using a conventional method like the Shinnar-Le Roux (SLR) algorithm [16].

2. If designing a standard one-photon pulse, directly set B_{xy} to the prototype pulse and finish.

3. Else if designing a multiphoton or corresponding frequency-modulated pulse, choose ω_z.

    a. Based on Eq. (26), choose values such that $B_{1,xy}(t) J_n\left(\frac{\gamma B_{1,z}(t)}{\omega_z}\right)$ equals the amplitude modulation of the prototype pulse, and $e^{-i\theta(t)} e^{-i\left(\frac{\gamma B_{1,z}(T)}{\omega_z}\sin(\omega_z T + \phi(T)) - n\phi(t)\right)} e^{-i\gamma\int_t^T B_{DC,z}(\tau)d\tau}$ equals the frequency modulation of the prototype pulse. A different equation instead of Eq. (26) may be used in specific situations, but the same principle of matching amplitude and frequency modulations applies. When either B_z or B_{xy} is chosen to be a hard pulse, they simply result in scaling factors.

    b. Shift the center frequency of the B_{xy} pulse by $n\omega_z$.

To generate each pulse for Figs. 5 and 6, no additional hardware for the scanner was used, and the specifics are described in Sections 3.5 and 3.6.

Brief details on each example pulse are compiled in Table 3.

3.2. Slice excitation by one-photon, two-photon, and frequency modulation

Using the above procedure, the first three sets of pulses were designed to show that equal slice profiles can be created in multiple ways. The first set used a one-photon pulse, a two-photon with constant-$B_{1,z}$ pulse, and a one-photon with frequency modulation pulse corresponding to the two-photon pulse, all designed to excite the same slice profile. The one-photon pulse was a SLR pulse generated using SigPy.RF [17]. The SLR pulse was designed to have a time-bandwidth product of 6 and a duration of 6 ms. The corresponding slice-select gradient was set to have an amplitude resulting in a 5 mm slice-thickness. A rewinder gradient was added to give the standard excitation k-space trajectory.

The two-photon pulse was designed following Eq. (16) using a hard B_z pulse. As Eq. (16) shows, when exciting the two-photon resonance, the hard B_z pulse effectively scales $B_{1,xy}$ by $J_1\left(\frac{\gamma B_{1,z}}{\omega_z}\right)$, but otherwise excites the same slice profile. So, to get the same flip angle as the one-photon pulse, the same $B_{1,xy}$ pulse as the one-photon pulse was used, except that it was scaled by $1/J_1\left(\frac{\gamma B_{1,z}}{\omega_z}\right)$. To excite the two-photon resonance instead of the one-photon resonance, the frequency of the B_{XY} pulse was also decreased by xz. Note that two-photon resonances can be excited with the frequency of the B_{xy} pulse either increased or decreased by ω_z. To make the B_z pulse more easily implementable, $\phi = -\pi/2$ to make it a sine wave that starts at zero instead of a cosine wave. The initial phase of h W:\Production\20042\025055MC\0001\Graphics was set to cancel out the resulting extra constant phase term given by $e^{-i\left(\frac{\gamma B_{1,z}}{\omega_z}\sin(\omega_z T + \phi) - n\phi\right)}$ in Eq. (16). Due to limitations in our amplifier's output power described later in Section 3.7, the $B_{1,z}$ amplitude was far from optimal, making $1/J_1\left(\frac{\gamma B_{1,z}}{\omega_z}\right)$ about 6.98 instead of the optimal value of 1.72. This and the other pulse parameters limited the maximum flip angle in our proof-of-concept implementation. Thus, a max of 30°was used for all example implemented single-slice pulses. See Supplementary Fig. 4 for simulations of 90° flip angles. The parameters and thus constraints, however, are different for the multislice pulses described later.

The one-photon frequency modulation pulse is a pulse where frequency modulation of the B_{xy} pulse imitates the effects of the B_z pulse. Specifically, in Eq. (11), the $e^{-i\theta(t)}$ term is set to be equal to the $e^{-i\gamma\int_t^T B_{1,z}(\tau)\cos(\omega_z\tau + \phi(\tau))d\tau}$ term from the two-photon pulse. $\theta(t)$ represents the phase/frequency modulation of the B_{xy} pulse. In this case, since the B_z pulse is a hard pulse, the integral can be directly evaluated, and so $\theta(t) = \frac{\gamma B_{1,z}}{\omega_z}(\sin(\omega_z T + \phi) - \sin(\omega_z t + \phi))$. Then, although there is no real B_z pulse, there is a fictitious one, so like for the two-photon pulse, $B_{1,xy}$ again needs to be multiplied by $1/J_1\left(\frac{\gamma B_{1,z}}{\omega_z}\right)$ to achieve the same flip angle as the original one-photon pulse. The major difference between the two-photon pulse and the frequency modulated pulse is that the two-photon pulse makes use of a real RF B_z field in the laboratory frame of reference while there does not exist one for the frequency modulated pulse in the laboratory frame of reference. As a result, despite its center frequency being offset by ω_z, the frequency modulated pulse actually has some frequency components at the Larmor frequency in the laboratory frame of reference while the two-photon pulse does not.

The designed pulses are shown in the first column of Fig. 2.

3.3.   Slice shifting with ω_{xy}, constant B_z, or ω_z

The second set of pulses dealt with slice shifting for a two-photon pulse, and equal shifts were designed using $\theta(t)$, $\mathrm{B}_{DC,z}(t)$, or $\Delta\omega$ in Eq. (18). All three pulses were the same two-photon pulse from Section 3.2, except shifted in position by the three methods. Setting $\theta(t) = \omega_{offset}t$, where ω_{offset} is some offset frequency, is the standard method of changing slice location by exciting a different local Larmor frequency along the slice-select gradient. From

the theory, changing the frequency of the B_{xy} pulse in a two-photon pulse shifts the slice position of the two-photon pulse by the same amount as it would for the corresponding one-photon pulse.

Instead of changing the B_{xy} pulse frequency, changing the local Larmor frequencies by adding a uniform near-DC magnetic field, $B_{DC,z}(t)$, is another method that has been historically used to change the excitation location. Here, we set $B_{DC,z}(t)$ to a constant during the excitation and removed it for the rest of the pulse sequence to show that again, the two-photon slice position changes the same amount as a one-photon slice position would.

Finally, changing $\Delta\omega$ in Eq. (18) to change slice position is unique to two-photon pulses. Instead of changing the B_{xy} pulse frequency, we can change the B_z pulse frequency by an equal amount to shift the slice. Just like in the B_{xy} pulse frequency case, changing the B_z pulse frequency excites a different local Larmor frequency along the slice-select gradient. When $\Delta\omega$ is not insignificant compared to ω_z though, Eq. (18) shows that the Bessel function scaling factor changes. So, in this case, $B_{1,xy}$ was multiplied by $1/J_1\left(\frac{\gamma B_{1,z}}{\omega_z + \Delta\omega}\right)$ instead.

The designed pulses are shown in the first column of Fig. 3.

3.4. Amplitude-modulated $B_{1,xy}$ and $B_{1,z}$ pulses

The third set of pulses was designed to show flexibility in choosing how the amplitude modulation can be split between $B_{1,xy}(t)$ and $B_{1,z}(t)$ based on Eq. (26). Because of the additional assumption of slow variation of $B_{1,z}(t)$ relative to ω_z used for deriving Eq. (26), the pulse length was increased from 6 ms to 24 ms to allow for slower $B_{1,z}(t)$ variation. Alternatively, ω_z could be increased instead, but our experimental setup did not allow for it, which will be elaborated more upon in Section 3.7. The first pulse in this set was the same as the second pulse from Section 3.2, except with a 24 ms duration instead of 6 ms.

The second pulse in this set moved all the amplitude modulation from $B_{1,xy}(t)$ to $J_1\left(\frac{\gamma B_{1,z}(t)}{\omega_z}\right)$. That is, $B_{1,xy}(t)$ was made a time-invariant hard pulse with an amplitude equal to the maximum of $B_{1,xy}(t)$ from the first pulse and $J_1\left(\frac{\gamma B_{1,z}(t)}{\omega_z}\right)$ was set to be a scaled version of $B_{1,xy}(t)$ as a function of time from the first pulse with the same maximum value of $B_{1,z}(t)$ as in the first pulse. Because $J_1\left(\frac{\gamma B_{1,z}(t)}{\omega_z}\right)$ is a nonlinear function of $B_{1,z}(t)$, a bounded optimization function from SciPy [18] was used to find the values of $B_{1,z}(t)$ needed to give the correct values of $J_1\left(\frac{\gamma B_{1,z}(t)}{\omega_z}\right)$ at every time point. As a result, the product $B_{1,xy}(t)J_n\left(\frac{\gamma B_{1,z}(t)}{\omega_z}\right)$, which is the total effective amplitude modulation of the two-photon pulse as shown in Eq. (26), was the same for the first and second pulses for all time.

The third pulse in this set was split into two halves. The first half had a hard pulse for $B_{1,xy}(t)$ while the second half had a hard pulse for $B_{1,z}(t)$. The product $B_{1,xy}(t)J_n\left(\frac{\gamma B_{1,z}(t)}{\omega_z}\right)$ was still the same for this pulse for all time, thus producing the same slice profile.

The designed pulses are shown in the first column of Fig. 4.

3.5.   Unequal-flip-angle multislice excitation and shifting

For the fourth set of pulses, the earlier uniform B_z field was replaced by linearly spatially varying oscillating gradients and the additional coil was removed. These oscillating gradients were added to a one-photon SLR pulse to demonstrate multislice excitation, and a spatially shifted version based on Eq. (31) was designed. The first pulse of this set was the same as the first pulse from Section 3.2, except 12 ms in duration and with an additional oscillating gradient of frequency 3 kHz superimposed on the slice-select gradient. The AC or oscillating component of the gradient was chosen to have an amplitude of 1.5 times the amplitude of the DC or slice-select component of the gradient. By choosing this ratio of amplitudes and using a hard pulse for the gradients, $\frac{\gamma(\mathbf{G}_{1,z} \cdot \mathbf{r})}{\omega_z} = 1.5$ at the two-photon resonance locations, $\frac{\gamma(\mathbf{G}_{1,z} \cdot \mathbf{r})}{\omega_z} = 3$ at the three-photon resonance locations, and so on. This is because as we move to higher order resonances, ω_z, the frequency of the z-photon provided by the oscillating gradients, remains the same while r, the position of the multiphoton resonance, gets multiplied by the number of z-photons involved as the local Larmor frequency changes with the DC component of the gradient and the resonance condition is at integer multiplies of ω_z offset from the isocenter Larmor frequency. A ratio of 1.5 was chosen because $J_1(1.5)$ and $J_2(3.0)$ are near the maximum points of $J_1(-)$ and $J_2(-)$ respectively. As a result, the two- and three-photon excitation bands are about 0.5 times as efficient as the one-photon band in terms of B_{xy} strength. However, as noted before, these extra multiphoton bands are excited using the same B_{xy} as the one-photon band, essentially being provided without extra RF energy deposition in a subject. Because SAR is proportional to $(fB_1)^2$, where f is the frequency of the RF, the RF energy deposition from the kilohertz oscillating gradients ($\mathbf{G}_{1,z}$ or $B_{1,z}$) is negligible, at least for our RF strengths. The total SAR savings depend on how many bands are used. For example, in the case of three bands and the gradient parameters chosen, integrating $B_{1,xy}^2$ for each pulse we have 0.62 times the SAR for the multiphoton pulse compared to an equivalent composed of three one-photon pulses scaled, shifted, and summed. In the case of five bands, we have 0.48 times the SAR for the multiphoton pulse compared to an equivalent composed of five one-photon pulses, scaled, shifted, and summed. The pulse length was set to 12 ms instead of 6 ms due to gradient slew rate limits. If the pulse were shorter, both the DC and AC parts of the gradient would be larger for the same time-bandwidth product and slice thickness. To prevent errors from discontinuous gradients, ϕ was set to $-\pi/2$ for a sine wave instead of a cosine wave. With $\omega_z T = 72\pi$ radians, this gives an extra linearly spatially varying phase described by $e^{-i\frac{\gamma \mathbf{G}_{1,z}(T) \cdot \mathbf{r}}{\omega_z}\sin(\omega_z T + \phi)}$ in eq. (30). To remove this, the rewinder gradient after the pulse was adjusted to give the opposite linearly spatially varying phase.

The second pulse of this set was the same as the first pulse, except that the frequency of the B_{xy} pulse was changed. This pulse was made to demonstrate that with the spatially non-uniform $B_{1,z}$ field provided by the oscillating gradients, shifting the slices is not the same as in Section 3.3. If the frequency of the B_{xy} pulse is changed, then the slices are

shifted, but the flip angles of each slice do not remain the same because the Bessel function order and/or the argument to the Bessel function changes at each excited slice.

The third pulse of this set demonstrates that based on Eq. (30), a spatially uniform $B_{1,z}(t)$ term can change the spatial zero point of $\mathbf{G}_{1,z}(t) \cdot \mathbf{r}$, thus making it as if the oscillating gradients were shifted in space. When this is used together with the standard shift of the frequency of the B_{xy} pulse from the second pulse in this set, then the slices are shifted with preserved flip angles. To show that this can be implemented without the extra hardware of an additional B_z coil, the B_{xy} pulse frequency modulation equivalent was used instead. That is, $\theta(t)$ was used to provide the same effect as a uniform $B_{1,z}(t)$ term as described in Section 3.2.

The designed pulses are shown in the first column of Fig. 5.

3.6. Equal-flip-angle multiphoton multislice excitation

Due to the differing multiphoton excitation efficiencies, the pulses in section 3.5 have unequal flip angles for each excited slice. However, by shifting and summing multiple scaled versions of multiphoton multislice pulses, we can achieve equal flip angles. For the fifth set of pulses, we show an example of this for three simultaneously excited slices. The designed pulses are shown in the first column of Fig. 6.

The first three rows of Fig. 6 individually show the pulses to be summed. The fourth row is a pulse created by the direct summation of the pulses from the first three rows, resulting in equal flip angles, and the fifth row is a pulse created by the naïve multislice method of summing three shifted single-slice SLR pulses without an oscillating gradient. The summed multiphoton multislice pulse has a clearly lower $B_{1,xy}$ amplitude than the naïve multislice pulse, and integrating $B_{1,xy}^2$ for each pulse we have 0.48 times the SAR for the summed three-slice multiphoton pulse compared to an equivalent composed of three one-photon pulses shifted and summed. Note that this is better than 0.62 times the SAR for three unequal flip angle slices from section 3.5 because the comparison one-photon pulse for three equal flip angle slices has greater SAR than the one-photon pulse for three unequal flip angle slices.

To get equal flip angles for the three slices of the summed multiphoton pulse, each pulse to be summed must be properly scaled. The left slice of the summed pulse is composed of the two-photon excitation of the first pulse (first row in Fig. 6), the one-photon excitation of the second pulse (second row in Fig. 6), and the three-photon excitation of the third pulse (third row in Fig. 6). The center slice is composed of the one-photon excitation of the first pulse, the two-photon excitation of the second pulse, and the two-photon excitation of the third pulse. The right slice is composed of the two-photon excitation of the first pulse, the three-photon excitation of the second pulse, and the one-photon excitation of the third pulse. Thus, to calculate the scalings of each pulse, if p_1 is the scaling of the first pulse, p_2 is the scaling of the second pulse, and p_3 is the scaling of the third pulse, then to get equal flip angles we must have $p_1 J_1(1.5) + p_2 J_0(0) + p_3 J_2(3.0) = p_1 J_0(0) + p_2 J_1(1.5) + p_3 J_1(1.5) = p_1 J_1(1.5) + p_2 J_2(3.0) + p_3 J_0(0)$. If we set $p_2 = p_3$ and add an additional normalization constraint that

$p_1 J_1(1.5) + p_2 J_0(0) + p_3 J_2(3.0) = 1$, then we can directly solve for the scaling factors as $p_1 = 0.43$ and $p_2 = p_3 = 0.51$.

The first row of Fig. 6 is the same as the first row of Fig. 5, except scaled by $p_1 = 0.43$. The second row of Fig. 6 is the same as the third row of Fig. 5, except scaled by $p_2 = 0.51$. The third row of Fig. 6 is the same as the third row of Fig. 5, except scaled by $p_3 = 0.51$ and shifted in the opposite direction. Again, the fourth row of Fig. 6 is the sum of the first three rows, and the fifth row of Fig. 6 is the sum of three individual single-slice pulses. For consistency with the previous examples, the flip angles were chosen to be 30°. Supplementary Fig. 5 is a 90° flip angle version of Fig. 6. Note that the flip angle is not constrained in the same way as for the single-slice pulses.

3.7. General pulse experimental implementation details

All experimental implementations were done on a GE 3T MR750w scanner (General Electric, Waukesha, WI, USA) with a liquid phantom, a GE 16-channel knee coil array for reception, and custom gradient echo sequences (GRE) written using the HeartVista platform (HeartVista, Inc., Los Altos, CA). The imaging plane was set to be perpendicular to the slice select axis to view slice profiles. An in-house built solenoid coil (18 in. diameter and 20 in. length with about 450 μH of inductance and 1 O of resistance) was used to generate a uniform B_z field [19] (Fig. 1). B_z waveforms were generated by a Siglent SDG6022X arbitrary waveform generator (Siglent Technologies Co., Ltd., Shenzhen, China) and amplified by an AE Techron 7224 amplifier (AE Techron, Inc., Elkhart, IN) in voltage-controlled current mode. The current from the amplifier was fed into the solenoid using a pair of 12 AWG speaker wires with speakON connectors that went through a waveguide from the console room into the scanner room. To easily allow for a nearly constant B_z pulse superimposed with the $B_{1,z}$ pulse, the coil was not tuned and matched. However, a high voltage 1000 pF chip capacitor (Manufacturer Product Number 222522K00102JQTAF9LM, Knowles Precision Devices, Norwich, United Kingdom) was placed in parallel with the coil near the output of the amplifier to reduce near-Larmor frequency noise and interference. This capacitor resonates with the coil, but at a frequency well above those used in this study.

To synchronize the B_{xy} and B_z pulses, a 7.5-cm-diameter copper loop on a PCB was used to simultaneously probe the B_{xy} and B_z fields. It was connected to an oscilloscope and the loop was oriented almost entirely in line with the B_z coil such that the induced voltage on the loop would be similar for both B_{xy} and B_z despite the orders of magnitude difference in frequencies. The delay times of the pulse sequence trigger and the waveform generator were adjusted until the B_{xy} and B_z pulses overlapped in time with a precision of 2μs. $B_{1,z}$ amplitudes were calibrated with a custom calibration program in HeartVista such that equivalent one- and two-photon pulses produced equal mean signal for the center one-fifth of a 1D projection. In detail, the scanner was programmed to repeatedly output excitations with 1D readouts using either just a standard one-photon B_{xy} pulse or a frequency-offset and scaled B_{xy} pulse with a trigger for the B_z pulse. The frequency-offset and scaled B_{xy} pulse was verified to produce no excitation without a simultaneous B_z pulse. For only the frequency-offset and scaled B_{xy} pulse, the pulse sequence triggered the waveform generator to generate

corresponding frequency B_z waveforms to the amplifier, which produced current into the B_z coil (Fig. 1). The output voltage scaling of the waveform generator was increased until the mean of the center one-fifth of the values of the Fourier transforms of the 1D readouts for both excitations were approximately equal to a precision of about 1%, limited by noise. Based on the fact that for the two-photon resonance, the B_{xy} pulse is effectively scaled by $1/J_1\left(\frac{\gamma B_{1,z}}{\omega_z}\right)$, the B_z max amplitude was determined to be about 0.17 mT at 25 kHz, which was limited by the amplifier. To prevent phase/frequency drifts between the scanner and the waveform generator, the waveform generator's clock was synchronized to the 10 MHz reference signal from the scanner. Although the amplifier was operated in voltage-controlled current mode, it was found that when used, the DC component of the B_z waveform from the waveform generator had higher gain than expected. So, it was experimentally reduced in magnitude compared to the AC component by decreasing it until the slice location for the second pulse in Fig. 3 was correct.

All $\omega_z/2\pi$ values used with the additional B_z coil were 25 kHz because the amplifier could not produce large enough $B_{1,z}$ amplitudes for use with practical $B_{1,xy}$ values at higher ω_z frequencies with this coil. Because of this relatively small ω_z value, the slice-select gradients were constrained to be relatively small in order to keep the frequency-offset B_{xy} pulses from exciting off-center slices in the phantom and fulfill the assumption that only a one or a two-photon resonance is significant. This translated to small time-bandwidth products or long RF pulses. Time-bandwidth products were also limited due to increasing peak $B_{1,xy}$ values with increasing time-bandwidth products. Since peak $B_{1,xy}$ values need to be scaled by $1/J_1\left(\frac{\gamma B_{1,z}}{\omega_z}\right)$ for two-photon pulses to achieve the same flip angle, small $B_{1,z}$ amplitudes make this scaling value large and potentially impractical.

Under informed, written consent and procedures approved by our institution's IRB, a healthy volunteer was scanned with the same GRE sequences as the phantom experiments to show the in-plane images resulting from the selective excitation for one- and two-photon excitation. The parameters of the in vivo scans were: TR/TE = 200/6.6 ms, FA = 10°, 20°, or 30°, FOV = 256×256 mm^2, matrix = 256×256, 1 slice of 5-min thickness, 125-kHz readout bandwidth, 53-sec scan time. For the two-photon pulses, 25 kHz $\omega_z/2\pi$, −25 kHz offsets to $\omega_{xy}/2\pi$, 0.17 mT $B_{1,z}$ amplitude, $B_{1,xy}$ was 6.98 times larger than for the corresponding one-photon pulses.

4. Results

4.1. Slice excitation by one-photon, two-photon, and frequency modulation

Fig. 2 shows the simulations and experimental results of the pulses described in Section 3.2. The first row corresponds to the one-photon pulse, the second row corresponds to the two-photon pulse, and the third row corresponds to the frequency-modulated one-photon pulse. The first column plots the excitation portion of the pulse sequence, the second column plots the simulated results of the excitation based on Eq. (1), and the third column shows the slice profile imaged via a plane perpendicular to the slice-select axis. A close-up view of a part of the excitation pulse sequence denoted by the dotted red lines is provided in the right

side of the first column, and a line plot of the intensity across the center of the slice profile image is also provided in the third column.

As shown in Fig. 2, one-photon, two-photon, and frequency-modulated one-photon pulses produce the same slice-selective excitation when designed to be equivalent. The simulated and experimental slice profiles appear as expected. The $|B_{xy}|$ values for the two-photon and frequency-modulation pulses are larger by a factor of $\dfrac{1}{J_1\left(\frac{1\,B_{1,z}}{\omega_z}\right)} = \dfrac{1}{J_1\left(\frac{42.58(170)}{25000}\right)} = 6.98$ by design to achieve the same flip angle as the one-photon pulse. If larger B_z values could be achieved, $\dfrac{1}{J_1\left(\frac{\beta_{1,z}}{\omega_z}\right)}$ could be as low as 1.72. See Supplementary Figs. 1 and 2 for simulated pulses with a 1.08 mT $B_{1,z}$ amplitude, which achieves $\dfrac{1}{J_1\left(\frac{\beta_{1,z}}{\omega_z}\right)} = 1.72$ for $\omega_z/2\pi = 25$ kHz.

4.2. Slice shifting with ω_{xy}, constant B_z, or ω_z

Fig. 3 shows the simulations and experimental results of the two-photon pulse from Fig. 2, except shifted in position by three different methods as described in Section 3.3. The first row corresponds to shifting via changing ω_{xy}, or equivalently a linear $\theta(t)$. The second row corresponds to shifting via $B_{DC,z}(t)$, and the third row corresponds to shifting via changing ω_z. The columns are analogous to Fig. 2. When a two-photon pulse is used, it can be shifted by a change in ω_{xy}, the addition of a constant B_z, or a change in ω_z. The changes in ω_{xy} and *ApexGraAbsGraphic* are small compared to ω_{xy} and ω_z, so the differences in the plots are a little difficult to spot. However, in the close-up views of the pulse sequences, the phases can be seen to slightly differ. For the second row with a constant B_z, note that the B_z subplot has a slight negative offset relative to the dotted lines representing zero field.

As shown in Fig. 3, the three ways of shifting the slice can produce equivalent shifts.

4.3. Amplitude-modulated $B_{1,xy}$ and $B_{1,z}$ pulses

Fig. 4 shows the simulations and experimental results of two-photon SLR pulses with a time-bandwidth product of 6 and a duration of 24 ms, as described in section 3.4. The first row corresponds to the pulse with amplitude modulation fully in the B_{xy} pulse, the second row corresponds to the pulse with amplitude modulation fully in the B_z pulse, and the third row corresponds to the pulse with amplitude modulation in both the B_{xy} and B_z pulses. Making the pulses have longer durations allows the assumption that the modulation of the B_z pulses is slow compared to the frequency ω_z to be better satisfied. Given the proper equipment, ω_z could have been increased by a few times instead of the duration of the pulse. See Supplementary Fig. 3 for simulated pulses with a duration of 6 ms and $\omega_z/2\pi = 150\text{kHz}$. All three pulses have essentially the same slice profile, but in the second and third row, some passband ripple can be seen. These ripples disappear with better satisfied assumptions as shown in Supplementary Fig. 3.

4.4. Unequal-flip-angle multislice excitation and shifting

Fig. 5 shows the simulations and experimental results for the multislice excitation pulses described in Section 3.5. The first row demonstrates the principle of getting free unequal slices by taking a base one-photon pulse like in the first row of Fig. 2 and adding an oscillating gradient waveform to the slice select gradient. This creates a spatially varying $B_{1,z}$ field. From the combination of the effects of a slice-select gradient and a spatially varying $B_{1,z}$ field, excitation occurs whenever multiphoton resonance conditions are met. Slices are excited whenever the local Larmor frequency determined by the slice-select gradient is offset from the xy-RF center frequency by an integer multiple of ω_z. Unlike in the previous examples, here we wanted multiple multiphoton resonances to be in the field of view instead of just one. The isocenter has a one-photon resonance. The two bands immediately adjacent are two-photon resonances, and if the field of view is large enough to contain them, the two after that are three-photon resonances, etc. For the first pulse in Fig. 5, despite B_{xy} being exactly the same as a single-slice SLR pulse, many extra excitation bands are created. The extra bands, however, have unequal excitations due to varying multiphoton excitation efficiencies.

As shown in the second pulse in the second row, shifting ω_{xy} does not equally shift all of the pulses. At the isocenter, because there is no $B_{1,z}$ field, there can only ever be a one-photon resonance. This can be fixed by either adding a uniform $B_{1,z}$ field such that the isocenter can have multiphoton resonances, or by using the corresponding frequency modulation of the B_{xy} pulse. The final pulse in Fig. 5 goes the frequency modulation route.

4.5. Equal-flip-angle multiphoton multislice excitation

Fig. 6 shows the simulations and experimental results for the mutlislice excitation pulses described in Section 3.6. The simulated and experimental slice profiles look as expected and the profiles of the summed multiphoton multislice pulse (row 4) and the naïve multislice pulse consisting of three individual one-photon single-slice pulses (row 5) look essentially the same. The multiphoton multislice pulse halves the SAR without any increase in pulse duration for the equivalent one-photon multislice pulse. While the excitation profiles produced by the multiphoton pulse were essentially the same as a one-photon 12 ms SLR pulse with a time-bandwidth product of 6, our choice of pulse duration was limited by the gradient slew rate, especially on our wide-bore scanner. The gradient slew rate requirement can be decreased by reducing the time-bandwidth product at the expense of worse slice profiles or by reducing the AC to DC gradient ratio at the expense of reduced SAR benefits. Decreasing the slice spacing also decreases the required gradient slew rate because the resonance conditions occur at lower ω_z values. As a potential downside, the multiphoton pulse also produces extra bands beyond the three center ones, which are not shown for clarity. Also, although it is very minor and not easily observable, because the $B_{1,z}$ field produced by the oscillating gradients is linearly varying within each slice, there may be slight variation in excitation efficiency within each slice, producing a slight ramp along the slice profile. This effect is somewhat cancelled out by the addition of multiple shifted pulses though.

4.6. In vivo one-photon and two-photon excitation

Using the same one-photon and two-photon pulses as in Fig. 2, Fig. 7 shows the in-plane results of the one-photon and two-photon pulses in vivo in three different orientations. Difference images are also given as one-photon minus two-photon for each pair. There is significant shading in the images because the same knee coil for reception used for the phantom experiments was wrapped around the head, and because the coil was designed for a knee, the coverage of the head was not complete. Since the body coil was used for RF transmit, the transmit field was relatively uniform. No significant differences between the images are visually observed for this set of parameters. To clearly show differences or the lack of them, linear registration in the Fourier domain was applied before subtraction in the image domain. The subtraction images are red for locations where one-photon was larger and blue for where two-photon was larger. The resulting differences are of similar order of magnitude to the background noise. SNR values were calculated for white matter regions of interests by taking the mean of at least 300 white matter voxels and dividing by the standard deviation of 10,000 background voxels. The results are tabulated in Table 2. The one- and two-photon SNR values are essentially the same, with any differences in SNR and the subtraction images potentially caused by inhomogeneity in the B_z coil. An optimized, more homogenous B_z coil is the subject of future work. Otherwise, the one-photon and two-photon images appear to be of similar quality. Overall, there is no significant unexpected effect in vivo with our parameters and excitation 25 kHz away from the Larmor frequency.

5. Discussion and conclusions

We describe the basic principles of multiphoton selective excitation by utilizing multiple magnetic fields controllable in all three axes. The analysis is based on the Bloch equations and results in an extension of the classical excitation k-space formulation [15] and beyond.

We showed that when ω_z is large enough, the distinction between the xy- and z-direction RF becomes smaller, and the ability to modulate B_z instead of B_{xy} gives extra flexibility to the multiphoton RF designer. We demonstrated how the same slice profiles can be achieved in many ways. For the simple case with a homogenous B_z coil and relatively low ω_z though, the use of a hard B_z pulse and modulation of B_{xy} usually optimizes SAR and pulse duration.

Setting SAR and pulse duration aside, the flexibility of multiphoton pulses can be used in more unique situations. Since multiphoton pulses do not have any RF at the Larmor frequency, a pulsed version of frequency-isolated simultaneous transmit and receive like in [11,20] could be implemented. In this case, it may be useful to modulate the B_z pulse instead of the B_{xy} pulse if a constant B_{xy} pulse makes the separation between the B_{xy} pulse and the received signal in the xy-direction easier, for example by subtraction. When designing a new scanner from the ground up, shimming coils or other coils that generate B_z fields to traditionally compensate for drifts in the B_0 field may add modulation to their duties, and in return, the traditional RF transmit signal chain may be reduced in complexity. In an extreme case, the traditional B_{xy} RF could simply only need to turn on and off, which is potentially useful if a very high Q coil is used at ultralow fields where SAR is less of a concern. The bandwidth of the B_{xy} coil can be effectively increased during a transmit pulse

by using B_z modulation while higher SNR from a high Q factor can be obtained during a low bandwidth signal readout. As another application, knowledge of B_{xy} RF field distributions and the theory described here can potentially allow one to measure unknown kHz frequency B_z fields in time and space.

In a more standard high-field setting, the benefits of multiphoton excitation emerge when non-uniform B_z fields are used together with multiple resonances, both one-photon and multiphoton. Although two-photon pulses were mainly used as examples, the theory shows that there are direct extensions to higher-order multiphoton pulses. The pulses in Figs. 5 and 6 exemplify this and show that by allowing non-uniform B_z fields, more spatially complex excitation can be achieved with reduced SAR and no increase in duration. Since multiphoton pulses can be easily designed based off of standard one-photon pulses, further SAR reduction with other methods such as VERSE [21] should be compatible. While the three-slice reduced SAR example in Fig. 6 is already directly applicable to simultaneous multislice [8–10] applications without extra hardware, even further reductions in SAR are potentially achievable with multiphoton parallel transmit and higher channel-count spatial encoding fields, for example by directly compensating for the non-uniformity of the pulse in Fig. 5 or by providing more optimally distributed $B_{1,z}$ fields over space. With high channel-count B_z and B_{xy} coils, individual coils may use different combinations of slice-shifting and modulation methods to achieve more optimal excitations (profile, uniformity, SAR, etc) in the presence of various spatial non-idealities such as B_0 and B_1 inhomogeneities. As shown in the theory, changes in $B_{z,DC}$, or alternatively changes in B_0, do the same exact thing to multiphoton pulses as they do to standard one-photon pulses. Since the equations also hold for $B_{z,DC}$ as a function of position, the effects of B_0 inhomogeneity are exactly the same for one-photon and multiphoton pulses. With the added flexibility of multiphoton pulses in combination with one-photon pulses, however, more can potentially be done to combat B_0 and B_1 non-idealities. Different slice-shifting and modulation methods may enable more spatial control because, even if they come from the same coil, B_z fields to change local B_0 fields may not have the same spatial profile as $B_{1,z}$ fields due to differing interactions between the object being imaged and the fields at different frequencies. Furthermore, if one coil can be used to produce both $B_{1,z}$ and $B_{1,xy}$ fields, then the spatial effects of modulating one versus the other will be very different simply due to one being a z-direction field and the other being a xy-direction field. Interestingly, due to the non-linear nature of multiphoton excitation, two-photon, three-photon, and higher order excitations will also all have different spatial excitation profiles for a non-uniform $B_{1,z}$ field originating from the same coil. Given optimization procedures that take into account all of these different ways of spatially controlling the excitation with different spatial profiles, we expect that custom arrays of coils able to produce both kHz and Larmor frequency fields will bring out more of multiphoton excitation's potential in MRI.

Data availability

The data/code is available at https://github.com/LiuCLab/multiphoton-selective-excitation.

Supplementary Material

Refer to Web version on PubMed Central for supplementary material.

Acknowledgements

Appendix.

Assumptions for shaped-$B_{1,z}$ pulse analysis

Let us discuss a little about the assumptions from Section 2.2.2. They are listed in the following.

1. $\int_t^T \frac{\sin(\omega_z \tau)}{\omega_z} \frac{d}{d\tau}[B_{1,z}(\tau)\cos(\phi(\tau))]d\tau$ is negligible compared to $\left[B_{1,z}(\tau)\cos(\phi(\tau))\frac{\sin(\omega_z \tau)}{\omega_z}\right]_t^T$.

2. $\int_t^T \frac{-\cos(\omega_z \tau)}{\omega_z} \frac{d}{d\tau}[B_{1,z}(\tau)\sin(\phi(\tau))]d\tau$ is negligible compared to $\left[B_{1,z}(\tau)\sin(\phi(\tau))\frac{-\cos(\omega_z \tau)}{\omega_z}\right]_t^T$.

3. The bandwidth of $J_m\left(\frac{\gamma B_{1,z}(t)}{\omega_z}\right)e^{im\phi(t)}$ is small relative to $(m-n)\omega_z$.

For more intuition on assumption 1, since it is a bit difficult to compare an integral with a value, we can apply integration by parts again to obtain

$$\int_t^T \frac{\sin(\omega_z \tau)}{\omega_z} \frac{d}{d\tau}[B_{1,z}(\tau)\cos(\phi(\tau))]d\tau$$
$$= \left[\frac{d}{d\tau}[B_{1,z}(\tau)\cos(\phi(\tau))]\frac{-\cos(\omega_z \tau)}{\omega_z^2}\right]_t^T - \int_t^T \frac{-\cos(\omega_z \tau)}{\omega_z^2}$$
$$\times \frac{d^2}{d\tau^2}[B_{1,z}(\tau)\sin(\phi(\tau))]d\tau$$

(A1)

For the first term on the right hand side of Eq. (A1) to be negligible, we want

$\frac{\frac{d}{d\tau}[B_{1,z}(\tau)\cos(\phi(\tau))]}{\omega_z^2} \ll \frac{B_{1,z}(\tau)\cos(\phi(\tau))}{\omega_z}$ or $\frac{\frac{d}{d\tau}[B_{1,z}(\tau)\cos(\phi(\tau))]}{\omega_z} \ll B_{1,z}(\tau)\cos(\phi(\tau))$ for all time. This

assumption becomes more reasonable as ω_z increases. For the second term, we can continue to expand it with integration by parts infinitely, obtaining more terms with higher and higher order derivatives. In the same spirit as the slowly varying amplitude approximation [22] often used in optics though, we can often directly consider these higher order derivatives to be negligible. Assumption 2 follows the same logic.

In order for assumption 3 to be true, $B_{1,z}(t)$ and $\phi(t)$ must be slowly varying such that the Fourier transforms of their relevant terms have negligible frequency components near $(m-n)\omega_z$, so that $e^{-in\omega_z t} J_m\left(\frac{\gamma B_{1,z}(t)}{\omega_z}\right) e^{im(\omega_z t + \phi(t))}$ only consists of fast oscillating components when m is not equal to n. Since J_m is a nonlinear function, generally, harmonics of $\frac{\gamma B_{1,z}(t)}{\omega_z}$ are produced and for the assumption to be true, these should also have negligible frequency components near $(m-n)\omega_z$. As long as the variation in $\frac{\gamma B_{1,z}(t)}{\omega_z}$ is relatively small though, the power in the harmonics generated by $J_m\left(\frac{\gamma B_{1,z}(t)}{\omega_z}\right)$ is also likely small. To make this assumption more easily satisfied, $J_m\left(\frac{\gamma B_{1,z}(t)}{\omega_z}\right)$ instead of $B_{1,z}(t)$ can be directly designed just like $B_{1,xy}(t)$. Then, with a target $J_m\left(\frac{\gamma B_{1,z}(t)}{\omega_z}\right)$, $B_{1,z}(t)$ can be solved for.

Note that unlike Eq. (18), the frequency/phase modulation of the B_z pulse in Eq. (26) does not appear inside the Bessel function. This is because in Eq. (26), the equivalent of $\omega_z \gg \Delta\omega$ is assumed.

References

[1]. Eles PT, Michal CA, Two-photon excitation in nuclear magnetic and quadrupole resonance, Progress Nucl. Magn. Reson. Spectrosc 56 (3) (2010), 10.1016/j.pnmrs.2009.12.002.

[2]. Michal CA, Nuclear magnetic resonance noise spectroscopy using two-photon excitation, J. Chem. Phys 118 (8) (2003), 10.1063/1.1553758.

[3]. Abragam A, The Principles of Nuclear Magnetism, Clarendon Press, 1961.

[4]. Boscaino R, Messina G, Double quantum coherent transients in a two-level spin system: A vectorial model, Physica B+C 138 (1–2) (1986), 10.1016/0378-4363(86)90506-1.

[5]. Eles PT, Michal CA, Two-photon two-color nuclear magnetic resonance, J. Chem. Phys 121 (20) (2004), 10.1063/1.1808697.

[6]. Zur Y, Levitt MH, Vega S, Multiphoton NMR spectroscopy on a spin system with I =1/2, J. Chem. Phys 78 (9) (1983), 10.1063/1.445483.

[7]. Han V, Liu C, Multiphoton magnetic resonance in imaging: A classical description and implementation, Magn. Reson. Med 84 (3) (2020), 10.1002/mrm.28186.

[8]. Larkman J, Hajnal JV, Herlihy AH, Coutts GA, Young IR, Ehnholm G, Use of multicoil arrays for separation of signal from multiple slices simultaneously excited, J. Magn. Reson. Imaging 13 (2) (2001), 10.1002/1522-2586(200102)13:2<313::AID-JMRI1045>3.0.CO;2-W.

[9]. Setsompop K, Gagoski BA, Polimeni JR, Witzel T, Wedeen VJ, Wald LL, Blipped-controlled aliasing in parallel imaging for simultaneous multislice echo planar imaging with reduced g-factor penalty, Magn. Reson. Med 67 (5) (2012), 10.1002/mrm.23097.

[10]. Barth M, Breuer F, Koopmans PJ, Norris DG, Poser BA, Simultaneous multislice (SMS) imaging techniques, Magn. Reson. Med 75 (1) (2016), 10.1002/mrm.25897.

[11]. Brunner D, Pavan M, Dietrich B, Rothmund D, Heller A, Pruessmann K, Sideband Excitation for Concurrent RF Transmission and Reception, in: Proceedings of the ISMRM Annual Meeting and Exhibition, 2011, p. 625.

[12]. Feynman RP, Vernon FL, Hellwarth RW, Geometrical Representation of the Schrödinger Equation for Solving Maser Problems, J. Appl. Phys 28 (1) (1957), 10.1063/1.1722572.

[13]. Joseph PM, Axel L, O'Donnell M, Potential problems with selective pulses in NMR imaging systems, Med Phys 11 (6) (1984) 772–777, 10.1118/1.595579. [PubMed: 6513885]

[14]. Bernstein MA, King KF, Zhou XJ, Handbook of MRI Pulse Sequences, Elsevier, 2004.

[15]. Pauly J, Nishimura D, Macovski A, A k-space analysis of small-tip-angle excitation, J. Magn. Reson (1969) 81 (1) (1989), 10.1016/0022-2364(89)90265-5.

[16]. Pauly J, Roux PL, Nishimura D, Macovski A, Parameter relations for the Shinnar-Le Roux selective excitation pulse design algorithm (NMR imaging), IEEE Trans. Med. Imaging 10 (1) (1991), 10.1109/42.75611.

[17]. Martin J, Ong F, Ma J, Tamir J, Lustig M, Grissom W, SigPy.RF: Comprehensive Open-Source RF Pulse Design Tools for Reproducible Research, in: Proceedings of the ISMRM Annual Meeting and Exhibition, 2020, p. 1045.

[18]. Virtanen P et al. , SciPy 1.0: fundamental algorithms for scientific computing in Python, Nat. Methods 17 (3) (2020) 261–272, 10.1038/s41592-019-0686-2. [PubMed: 32015543]

[19]. Chi J, Han V, Liu C, In vivo Two-photon Magnetic Resonance Imaging of Human Brain at 3T, in: Proceedings of the ISMRM Annual Meeting and Exhibition, 2021, p. 0564.

[20]. Brunner DO, Dietrich BE, Pavan M, Prüssmann KP, MRI with Sideband Excitation: Application to Continuous SWIFT, in: Proceedings of the ISMRM Annual Meeting and Exhibition, 2012, p. 150.

[21]. Conolly S, Nishimura D, Macovski A, Glover G, Variable-rate selective excitation, J. Magn. Reson 78 (3) (1988) 440–458, 10.1016/0022-2364(88)90131-X.

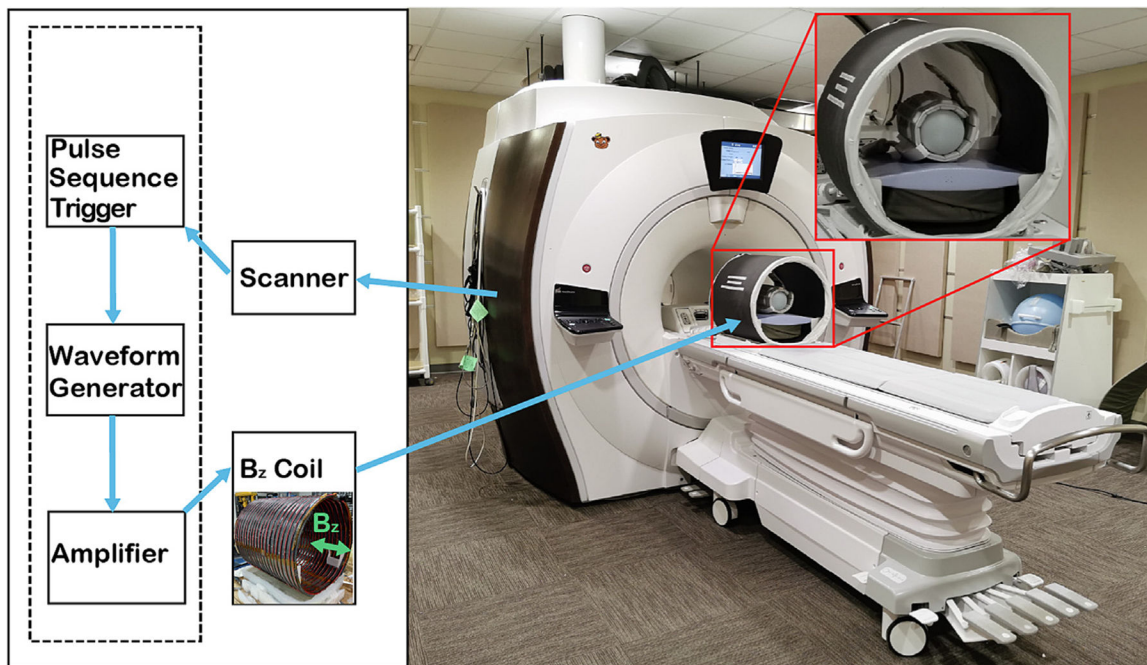[22]. Boyd RW, Nonlinear Optics, 4th edition., Academic Press, 2020.

Fig. 1. MRI System Setup with a B_z Coil.

For experiments that need a uniform B_z field, the pulse sequence triggers a waveform generator. The output of the waveform generator gets amplified by an amplifier in voltage-controlled current mode, and the current goes to a big solenoid, which produces a magnetic field in the same direction as B_0. A smaller picture of the solenoid before it was encased is shown on the left. A knee coil for reception wraps arounds a phantom inside the solenoid. The body coil is used for B_{xy} transmit.
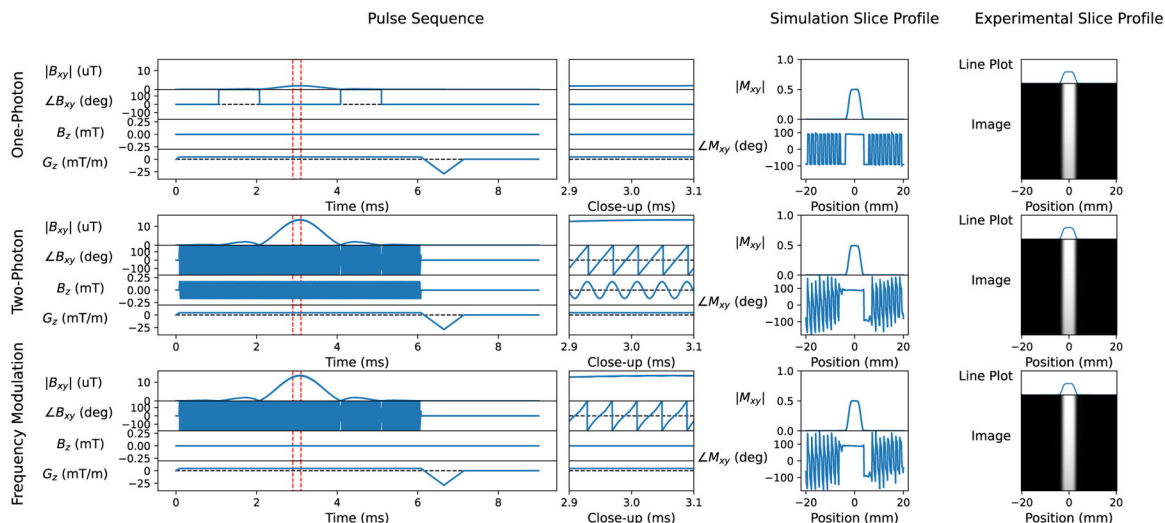
Fig. 2. Waveforms, Simulations, and Results for Corresponding One-photon, Two-photon, and Frequency Modulation Pulses.

The excitation pulse sequence, simulation, and experimental results are shown for corresponding one-photon, two-photon, and frequency modulated one-photon pulses. The dotted red lines indicate where the close-up view of the pulse sequence is. From the close-up, the frequency modulation of the final pulse can be more easily seen. All pulses are 5 mm slice thickness and have a time-bandwidth product of 6. The profiles are the same in both simulation and experiment. (For interpretation of the references to colour in this figure legend, the reader is referred to the web version of this article.)
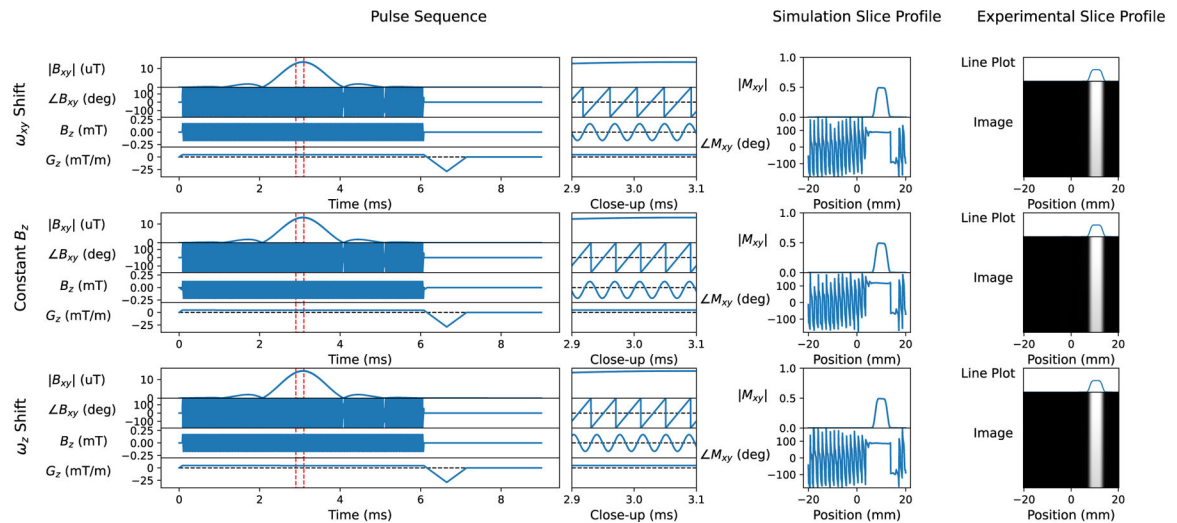
Fig. 3. Waveforms, Simulations, and Results for Corresponding Slice Position Shifts with ω_{xy}, Constant B_z, or ω_z.

The excitation pulse sequence, simulation, and experimental results are shown for equivalent slice shifts using a change in ω_{xy}, a DC B_z field, and a change in ω_z. The dotted red lines indicate where the close-up view of the pulse sequence is. From the close-ups, the first pulse has a slightly slower B_{xy} phase variation, the second pulse has a slight negative DC offset with a ramp at the end in the B_z field, and the third pulse has a slightly higher ω_z. The first pulse uses a slower phase variation because ω_{xy} was originally shifted to be lower than the Larmor frequency for this two-photon excitation. So, to increase the slice position, an increase in ω_{xy} means a slower phase variation in the Larmor frequency rotating frame. (For interpretation of the references to colour in this figure legend, the reader is referred to the web version of this article.)
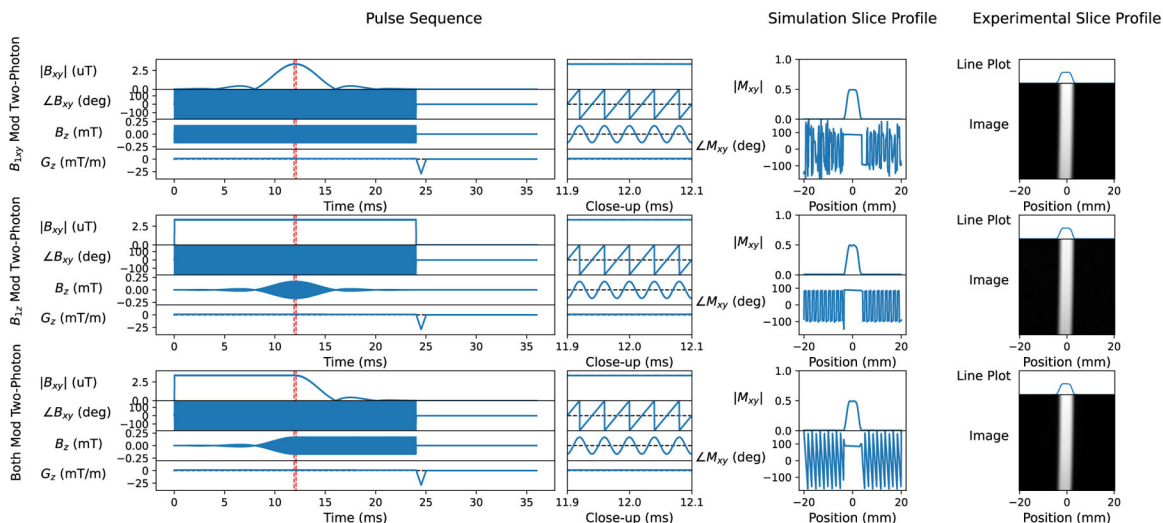
Fig. 4. Waveforms, Simulations, and Results for Corresponding Pulses Using Modulation in $B_{1,xy}$, $B_{1,z}$, or Both.

The excitation pulse sequence, simulation, and experimental results are shown for equivalent two-photon pulses with modulation in $B_{1,xy}$, $B_{1,z}$, or both. With the longer pulse duration, the oscillations on $B_{1,z}$ are no longer easily visible, thus better satisfying the assumption that modulation on $B_{1,z}$ is slow compared to ω_z. The dotted red lines indicate where the close-up view of the pulse sequence is. In the close-ups, it can be seen that B_z is still indeed oscillating, and that ω_{xy} is still offset by the same amount. (For interpretation of the references to colour in this figure legend, the reader is referred to the web version of this article.)
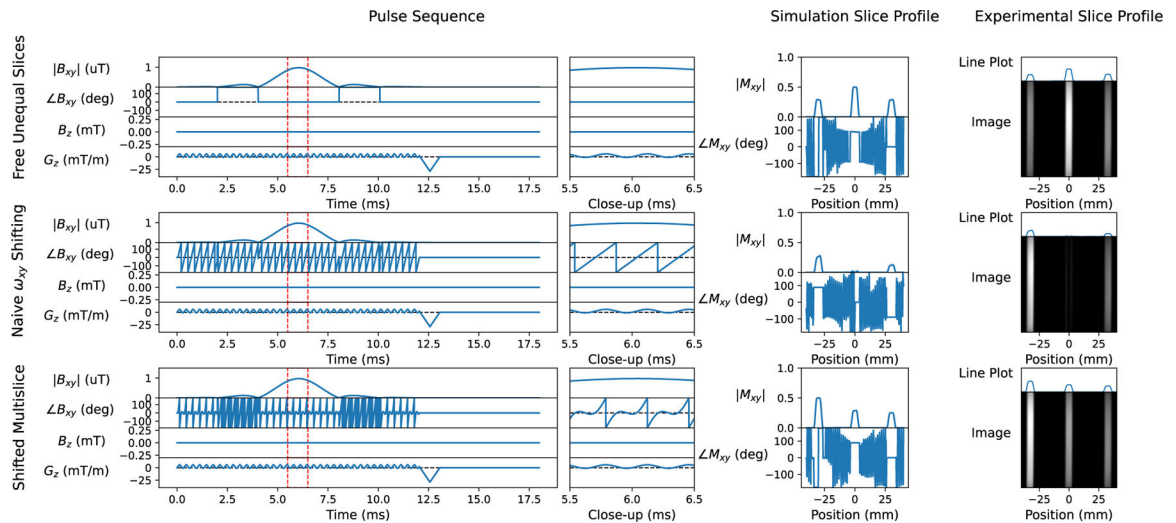
Fig. 5. Oscillating Gradients Generate Free Extra Slices, Which Should Be Shifted Using Both a Change in ω_{xy} and Frequency Modulation or a $B_{1,z}$ Pulse.

The excitation pulse sequence, simulation, and experimental results are shown for simple unequal flip angle multislice pulses. The first row is the same pulse from the first row of Fig. 2, but with a duration of 12 ms and the addition of an oscillating gradient to produce extra bands for free. The second row shows that simply changing ω_{xy} does not uniformly shift the bands. To properly shift the bands, as shown in the third row, a uniform $B_{1,z}$ or the equivalent frequency modulation of B_{xy} as used here is needed.
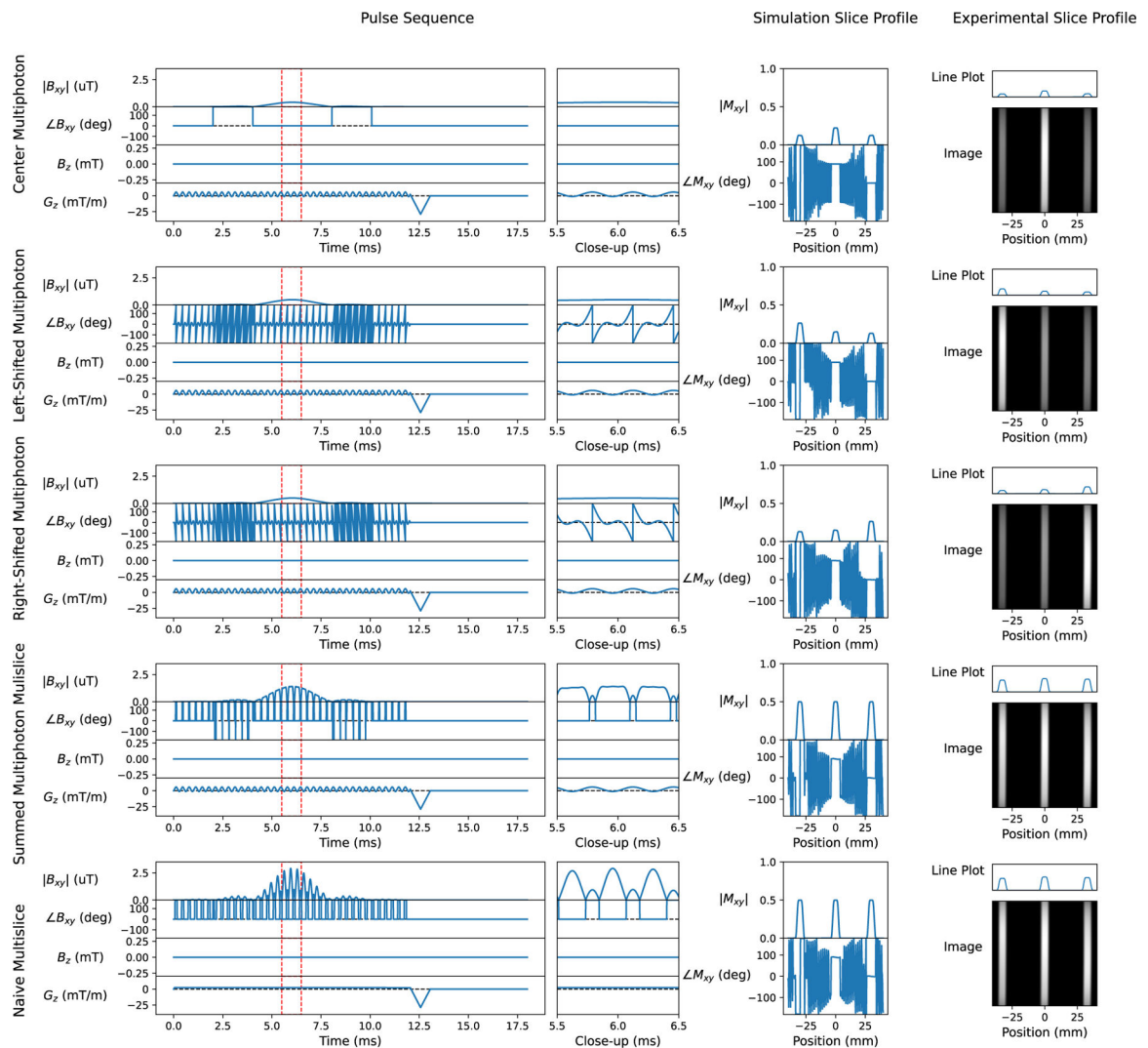
Fig. 6. Summing Shifted and Scaled Multiphoton Multislice Pulses Results in Equal Flip Angle Reduced SAR Multislice Pulses.

The first three rows are shifted and scaled versions of the first row from Fig. 5. The summation of these three pulses is shown in the fourth row. The fifth row shows a comparison pulse created by summing three standard single-slice pulses. The summed multiphoton multislice pulse of the fourth row has a clearly lower $B_{1,xy}$ amplitude compared to the naïve multislice pulse of the fifth row. In fact, the SAR of the multiphoton pulse is half that of the naïve multislice pulse.
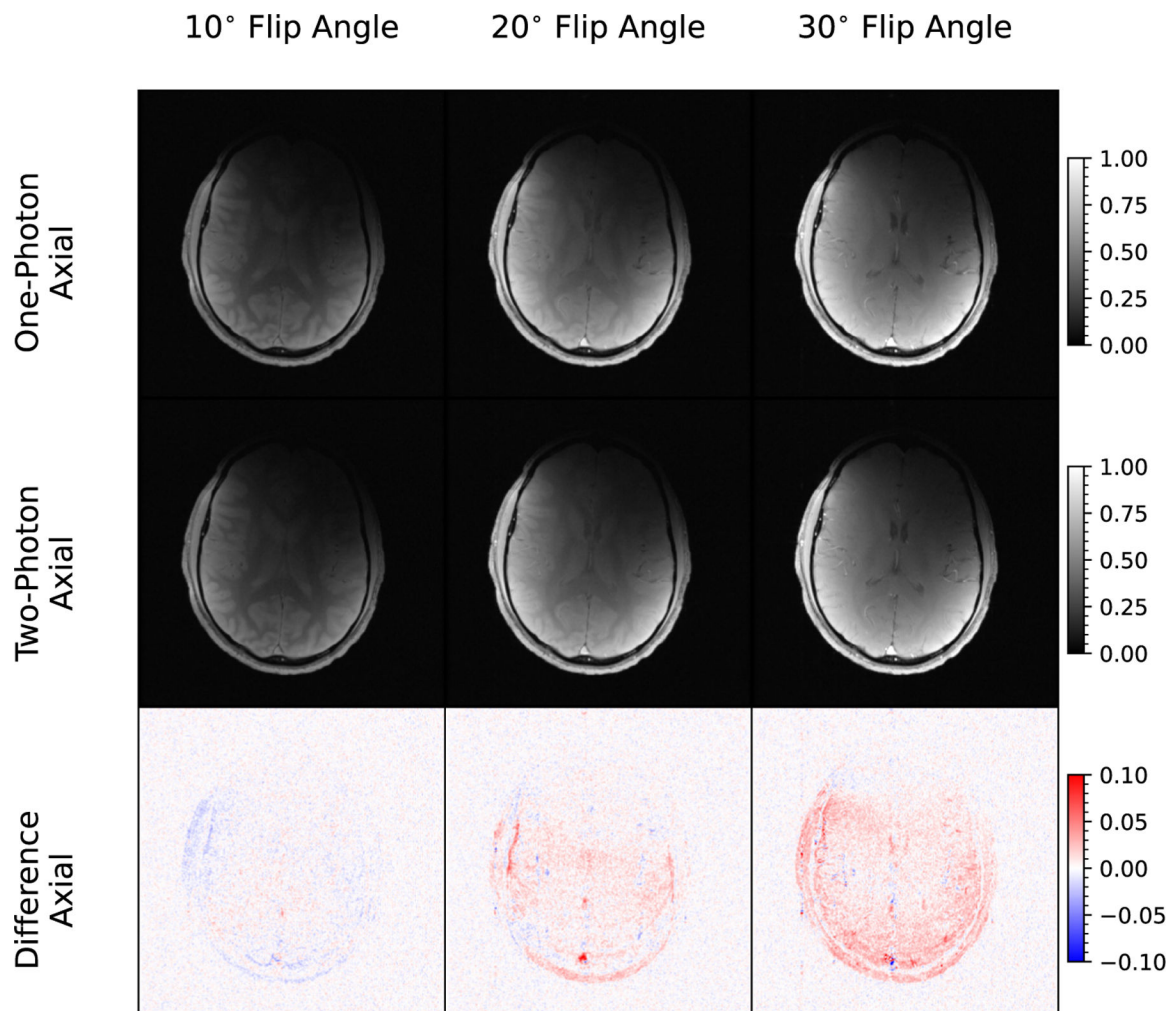
Fig. 7. In Vivo Single- and Two- Photon Selective Excitations Produce Similar Images When Designed to be Equivalent.

The same single- and two-photon selective excitation pulses from Fig. 2 were used for slice-selective in-plane imaging of a healthy volunteer. 10, 20, and 30°flip angles are shown. The maximum flip angle was limited by the peak $B_{1,xy}$ amplitude required for the given pulse parameters and maximum $B_{1,z}$ amplitude available. Difference images are red for greater signal in one-photon scans and blue for greater signal in two-photon scans. (For interpretation of the references to colour in this figure legend, the reader is referred to the web version of this article.)

Table 1

Variable Definitions.

Variable	Definition
M_x, M_y, M_z	Magnetization vector components
M_0	Equilibrium magnetization
B_x, B_y	Transverse magnetic field vector components
B_0	Main static magnetic field strength
T_1, T_2	Longitudinal and transverse relaxation times
T	Duration of RF pulse
γ	Gyromagnetic ratio
m_{xy}	Transverse magnetization vector in complex notation
B_{xy}	Transverse magnetic field in complex notation
$B_{1,xy}$	Amplitude of transverse RF magnetic field
B_z	Total longitudinal magnetic field
$B_{1,z}$	Amplitude of longitudinal RF magnetic field
$B_{DC,z}$	Uniform near-DC longitudinal magnetic field
ω_0	Larmor frequency (γB_0)
ω_z	Longitudinal RF angular frequency
$\Delta\omega$	Shift in longitudinal RF angular frequency
ω_{xy}	Transverse RF angular frequency
ϕ	Longitudinal RF extra phase
θ	Transverse RF extra phase
$\mathbf{G}$	Gradient vector for spatial encoding
$\mathbf{G}_{1,z}$	Oscillating component of gradient vector for excitation
$\mathbf{k}$	Excitation k-space vector
$J_m(-)$	Bessel function of the first kind of order m

Table 2

White Matter SNR for In Vivo Scans.

Image	SNR
One-Photon Axial (10° FA)	31.2
Two-Photon Axial (10° FA)	31.5
One-Photon Axial (20° FA)	52.3
Two-Photon Axial (20° FA)	51.6
One-Photon Axial (30° FA)	62.2
Two-Photon Axial (30° FA)	62.0
One-Photon Sagittal (10° FA)	37.8
Two-Photon Sagittal (10° FA)	37.7
One-Photon Sagittal (20° FA)	57.9
Two-Photon Sagittal (20° FA)	59.8
One-Photon Sagittal (30° FA)	62.9
Two-Photon Sagittal (30° FA)	65.5
One-Photon Coronal (10° FA)	24.4
Two-Photon Coronal (10° FA)	24.5
One-Photon Coronal (20° FA)	40.4
Two-Photon Coronal (20° FA)	39.5
One-Photon Coronal (30° FA)	47.7
Two-Photon Coronal (30° FA)	47.0

Table 3

Compilation of Pulse Examples and Properties.

Figure (Num. Row)	Type	Duration (ms)	Flip Angle (°)	Time-Bandwidth Product	Relative SAR from $B_{1;xy}$	Extra Hardware	Notes
2.1	One-Photon	6	30	6	1.0	No	Standard SLR
2.2	Two-Photon	6	30	6	49	Yes	$1/J_1\left(\frac{\gamma B_{1,z}}{\omega_z}\right)$ instead of optimal 1.72
2.3	Freq Mod	6	30	6	49	No	Frequency modulation equivalent of 2.1
3.1	Two-Photon	6	30	6	49	Yes	Shifted version of 2.2 by changing ω_{xy}
3.2	Two-Photon	6	30	6	49	Yes	Shifted version of 2.2 by adding constant B_z
3.3	Two-Photon	6	30	6	57	Yes	Shifted version of 2.2 by changing ω_z
4.1	Two-Photon	24	30	6	12	Yes	Constant $B_{1,z}$, modulated $B_{1,xy}$
4.2	Two-Photon	24	30	6	83	Yes	Modulated $B_{1,z}$, constant $B_{1,xy}$ version of 4.1
4.3	Two-Photon	24	30	6	48	Yes	Modulated $B_{1,z}$, modulated $B_{1,xy}$ version of 4.1
5.1	Multiphoton SMS	12	30, Various	6	0.50	No	Same SAR as a 12 ms, 30°, 6 TBW pulse, but extra unequal bands for free
5.2	Multiphoton SMS	12	Various	6	0.50	No	Example showing how not to shift 5.1
5.3	Multiphoton SMS	12	30, Various	6	0.50	No	Example showing shifting 5.1 by changing ω_{xy} and doing frequency modulation
6.1	Multiphoton SMS	12	Various	6	0.09	No	Same as 5.1, but scaled down
6.2	Multiphoton SMS	12	Various	6	0.13	No	Shifted and scaled version of 5.1
6.3	Multiphoton SMS	12	Various	6	0.13	No	Shifted and scaled version of 5.1
6.4	Multiphoton SMS	12	30	6	0.73	No	Sum of 6.1, 6.2, 6.3
6.5	One-Photon SMS	12	30	6	1.5	No	One-photon equivalent of 6.4
7	Two-Photon	6	10, 20, 30	6	49 for 30° pulse	Yes	Axial in-vivo demonstration of 2.2
S1.1	One-Photon	6	30	6	1.0	No	Repeat of 2.1
S1.2	Two-Photon	6	30	6	3.0	Yes	$1/J_1\left(\frac{\gamma B_{1,z}}{\omega_z}\right) = 1.72$ version of 2.2
S1.3	Freq Mod	6	30	6	3.0	No	$1/J_1\left(\frac{\gamma B_{1,z}}{\omega_z}\right) = 1.72$ version of 2.3
S2.1	One-Photon	1.4	30	6	4.3	No	Shorter version of 2.1

Figure (Num. Row)	Type	Duration (ms)	Flip Angle (°)	Time-Bandwidth Product	Relative SAR from $B_{1;xy}$	Extra Hardware	Notes
S2.2	Two-Photon	1.4	30	6	13	Yes	Shorter version of 2.2 using $1/J_1\left(\frac{\gamma B_{1,z}}{\omega_z}\right) = 1.72$
S2.3	Freq Mod	1.4	30	6	13	No	Shorter version of 2.3 using $1/J_1\left(\frac{\gamma B_{1,z}}{\omega_z}\right) = 1.72$
S3.1	Two-Photon	6	30	6	3.0	Yes	Shorter version of 4.1 using $\omega_z/2\pi = 150 kHz$ and $1/J_1\left(\frac{\gamma B_{1,z}}{\omega_z}\right) = 1.72$, which may lead to non-negligible SAR from $B_{1,z}$
S3.2	Two-Photon	6	30	6	20	Yes	Shorter version of 4.2 using $\omega_z/2\pi = 150 kHz$ and $1/J_1\left(\frac{\gamma B_{1,z}}{\omega_z}\right) = 1.72$
S3.3	Two-Photon	6	30	6	12	Yes	Shorter version of 4.3 using $\omega_z/2\pi = 150 kHz$ and $1/J_1\left(\frac{\gamma B_{1,z}}{\omega_z}\right) = 1.72$
S4.1	One-Photon	6	90	6	10	No	Larger flip angle version of 2.1
S4.2	Two-Photon	6	90	6	28	Yes	Larger flip angle version of 2.2 using $1/J_1\left(\frac{\gamma B_{1,z}}{\omega_z}\right) = 1.72$
S4.3	Freq Mod	6	90	6	28	No	Larger flip angle version of 2.3 using $1/J_1\left(\frac{\gamma B_{1,z}}{\omega_z}\right) = 1.72$
S5.1	Multiphoton SMS	12	Various	6	0.89	No	Larger flip angle version of 6.1 using base SLR pulse designed for 90°
S5.2	Multiphoton SMS	12	Various	6	1.3	No	Larger flip angle version of 6.2 using base SLR pulse designed for 90°
S5.3	Multiphoton SMS	12	Various	6	1.3	No	Larger flip angle version of 6.3 using base SLR pulse designed for 90°
S5.4	Multiphoton SMS	12	90	6	7.0	No	Larger flip angle version of 6.4 using base SLR pulse designed for 90°
S5.5	One-Photon SMS	12	90	6	14	No	Larger flip angle version of 6.5 using SLR pulse designed for 90°
S6	Two-Photon	6	10, 20, 30	6	49 for 30° pulse	Yes	Sagittal in-vivo demonstration of 2.2
S7	Two-Photon	6	10, 20, 30	6	49 for 30° pulse	Yes	Coronal in-vivo demonstration of 2.2